Novel measurement technique for the electromagnetic characterization of coating materials in the sub-THz frequency range

Andrea Passarelli,[*] Hannes Bartosik, and Giovanni Rumolo
CERN, 1211 Geneva 24, Switzerland

Vittorio Giorgio Vaccaro, Maria Rosaria Masullo, and Can Koral
INFN Naples Unit, 80126 Napoli, Italy

Gian Paolo Papari and Antonello Andreone
Physics Department, University of Naples Federico II and INFN Naples Unit, 80126 Napoli, Italy

Oliver Boine-Frankenheim
Technische Universität Darmstadt, Schlossgartenstraße 8, 64289 Darmstadt, Germany

This paper describes a reliable, handy, and inexpensive measurement system to characterize, in the sub-THz frequency range, the coating materials used in the beam pipes of accelerators. The method is based on time domain measurements of an electromagnetic wave passing through a waveguide having a thin central slab, where the coating material is deposited on both sides. Two horn antennas are integrated on both sides of the device to optimize the signal collection and detection. This novel technique is tested on slabs coated with a nonevaporable getter (NEG) and allows to evaluate the surface impedance in the frequency range from 0.1 to 0.3 THz.

I. INTRODUCTION

Modern accelerators and light sources often require special treatment of the vacuum chamber surface in order to avoid undesirable effects and to maximize machine performance. For example, the electron cloud in positron rings is a mechanism that starts when the synchrotron radiation, emitted by the beam, creates a large number of photoelectrons at the chamber wall surface. These primary electrons may hit the inner wall of the beam pipe, causing secondary emission or being elastically reflected [1]. If the secondary electron yield (SEY) of the surface material is greater than unity, the number of electrons grows exponentially leading to beam instabilities and many other side effects [2,3]. In order to reduce the SEY value in the pipe walls, a-C coatings have been extensively tested [4] and used [5] at the CERN SPS accelerator and other experiments [6] with very effective results.

Furthermore, ultrahigh vacuum is needed in particle accelerators to reduce the beam-gas scattering, the risk of high voltage discharge and to improve the thermal insulation [7].

The application of NEG coatings allows a distributed and continuous pumping in vacuum chambers of large accelerators even in very narrow beam pipes. CERN pioneered NEG thin film coating technology [8], which is nowadays widely used in many other accelerator facilities [9].

These coatings, exploited for the SEY reduction or for improvement of the pumping process, change the vacuum chamber surface impedance. The electromagnetic interaction of the beam with the surrounding vacuum chamber can result in beam instability limiting the performance of the machine. The electromagnetic characterization (EMC) of coating materials is therefore fundamental to build a reliable impedance model and to characterize performance limitations of modern particle accelerators and storage rings [10]. For example, the Compact Linear Collider (CLIC) requires very short bunches and therefore a thorough study of the surface impedance at very high frequencies (millimeter waves and beyond) is needed.

Experimental estimation of the surface impedance can be carried out by using two different methodologies: resonant cavity and transmission/reflection measurements [11,12]. The first one is very accurate albeit narrow band and often quite expensive due to the customized set of samples in terms of size, shape, etc. [13]. The second one is a broadband characterization technique that uses coaxial cables or waveguides or free-space, with a frequency band depending on the device used and on the instrumentation. The waveguide method [14] is usually simpler to use with

---

[*]Also at TEMF, TU Darmstadt.

respect to a coaxial cable where sometimes a complicated manufacturing of samples is needed, and does not require electrically large sizes as in the free space case. Waveguides are extensively used up to tenth of GHz for electromagnetic characterization of thick (compared to skin depth) or superconducting samples [15,16].

At higher frequencies, in the sub-mm-wave and mm-wave regions, the determination of coating material properties is usually done using time domain THz reflectometry [17]. However, this technique allows local measurements only (over a surface determined by the beam size) and becomes cumbersome when large area samples must be investigated. Besides that, in case of multilayered samples, the extraction of the intrinsic parameters and from here the impedance value is not so straightforward and is somehow model dependent [18].

THz waveguide spectroscopy is offering an alternative approach for materials that require a strong wave-matter interaction [19]. Until now, this technique has been used to characterize thin samples deposited or on dielectric substrates or directly in the waveguide [20,21].

Recently, frequency characterization of different NEG samples deposited on the lateral walls of a calibrated millimeter waveguide has been carried out by using two port VNA measurements [22,23]. However, this approach has some relevant drawbacks: (1) the nonhomogeneous deposition with unpredictable thickness and relevant peel-off and blistering; (2) the impossibility to reuse the system for further measurements on different coating materials; (3) the difficulty to extend the technique to larger area coating and at higher frequencies.

Our paper describes a novel measurement method for the EMC of materials used for the coating of accelerator beam pipes, aimed to overcome the inconveniences reported in the previous works. The solution proposed is to put a calibrated waveguide with integrated horn antennas in the optical path of a THz spectrometer and to separate the signal guiding system in two parts: one fixed (a circular waveguide), and one removable (a thin slab) where the coating is deposited. This choice allows to measure with ease large area coating deposited on metallic plates as in the case of accelerators, where averaged quantities are needed.

In the following we describe the waveguide design and the THz setup, the analytical method we use for the extraction of the material electromagnetic response, and the measurements performed on high quality NEG samples in order to validate the method. We believe that this approach may represent a first step to develop a reliable, handy and inexpensive system for measuring the surface impedance of coating materials in the very high frequency region.

II. METHOD

The proposed method is based on time domain measurements of an electromagnetic wave propagating inside a specifically designed waveguide (see Fig. 1), which has a
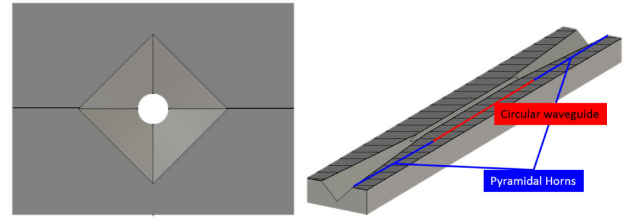

FIG. 1. DUT: circular waveguide and two pyramidal horns. Left: Front view. Right: Perspective view of longitudinal cut.

thin central copper slab where the material under test is deposited on both sides. Two horn antennas are integrated on both sides of the device to optimize the signal collection and detection. The waveguide is placed in the optical path of a THz spectrometer, as described in detail in Sec. IV. The conductivity value of the coated material is then obtained from the comparison between the signal amplitude transmitted through the waveguide with the coated slab and the one obtained with an uncoated slab used as a reference. Knowing the coating thickness and resorting to our analytical tool, the surface impedance can be inferred.

We assume that the measured electric field signals have the following expressions:

$$E_t^{cu}(f) = K(f)e^{-\alpha^{cu}(f)} \qquad (1)$$

$$E_t^{coat}(f) = K(f)e^{-\alpha^{coat}(f)} \qquad (2)$$

where α^{cu} and α^{coat} are the attenuation per unit length for the copper and the coated material respectively and $K(f)$ is the excitation coefficient. By expressing their ratio in dB:

$$\left[\frac{E_t^{cu}(f)}{E_t^{coat}(f)}\right]_{dB} = [\alpha^{coat}(f) - \alpha^{cu}(f)]20\log_{10}e \qquad (3)$$

one can retrieve the attenuation given by the coating material only, getting rid of the unknown excitation coefficient. As described later, the result of the measurements is compared to the analytical evaluation of the mode propagation in the device under test (DUT). The reliability of the analytical tool is tested by a comparison with numerical simulations performed using a commercial electromagnetic tool (CST Microwave Studio) [24]. The waveguide used for the experiment and the longitudinal cut where the slab is placed are described in detail in Sec. II A.

A. The device under test

A sketch of the device used for the experiment is shown in Fig. 1. It is composed by a circular waveguide connected to a pyramidal horn antenna on both sides, in order to enhance the electromagnetic signal collection and radiation [25]. These geometries have been chosen because of their low mechanical complexity, in terms of milling and drilling. Furthermore, the transition from the horns to the waveguide
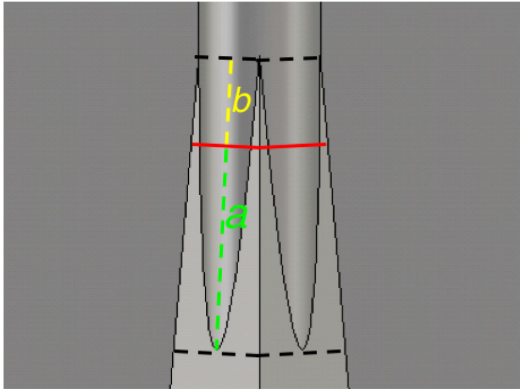
FIG. 2. Magnified top view of the transition between the pyramidal horn and the cylindrical waveguide. The red line indicates the cross section where the horn antenna ends and the cylindrical waveguide starts in the analytical model. a and b are the distances of the cross section from the apex and the cusp respectively of each ellipse (see text in Sec. II B).

is extremely smooth, as it can be observed at the magnified stretch in Fig. 2, where the transition curves are branches of very flat ellipses.

The external shape of the DUT is a parallelepiped of $16 \times 12 \times 120$ mm^3. The internal dimensions are reported in Table I. For the pyramidal horn, the maximum and minimum side along its length are indicated. The slab has the same length as the DUT (120 mm) and is 0.050 mm thick. During the deposition process, in order to prevent the deformation, the slab is held in an aluminum frame (see Fig. 3).

The NEG growth process was performed at the CERN deposition facilities on both sides of two different copper slabs by using a DC magnetron sputtering technique [4]. Measurements of thickness and alloy composition of the coating deposition along the median line of the slab (coincident with the waveguide axis) were performed using x-ray fluorescence (XRF). These measurements gave for the two slabs a mean thickness of 3.96 μm and 3.68 μm respectively (see Fig. 4), confirming the goodness of the uniformity of the coating. The evaluated average percentage of Titanium, Zirconium and Vanadium in the coating is 31%, 36.5%, and 32.5% for the first sample and 30.5%, 37%, and 32.5% for the second one (see Fig. 5).

B. Modes propagating in the DUT

A simplified analytical model can be built considering the loss contribution given by a single mode propagating

TABLE I. Waveguide internal dimensions.

	Length [mm]	Radius/Side [mm]
Cylindrical waveguide	42	0.9
Pyramidal horn	39	$6 \rightarrow 0.9\sqrt{2}$

FIG. 3. Top view of the longitudinal copper slab surrounded by the aluminum frame used during the NEG deposition. The four holes are for the correct alignment of the coated slab in the DUT during THz measurements.

inside the waveguide. In order to analytically model the horn-to-waveguide transition, we need to locate a plane orthogonal to the longitudinal axis where the pyramidal horn ends and the cylindrical waveguide starts. The distance a of this cross section from the apex of each ellipse is assumed to be two times the distance b to the ellipse cusps (see Fig. 2). This choice translates in a negligible transition contribution to the overall losses [26].

The presence of a slab placed in the median plane together with the incident wave conformation (quasiplane wave) select the modes that can propagate inside the waveguide. The electric field must be orthogonal and continuous (top-bottom) to the slab surface. Furthermore, left-right symmetries have to be satisfied. In other words: the projection of the incident plane wave on the mode must be non-zero.

The first allowed mode propagating inside the circular waveguide of the DUT is the $TE_{1,1}$ as shown in Fig. 6 [27]. The second mode is $TE_{1,2}$. All the other modes in between are forbidden by the boundary conditions and the symmetry. Therefore, the allowed bandwidth for the first mode
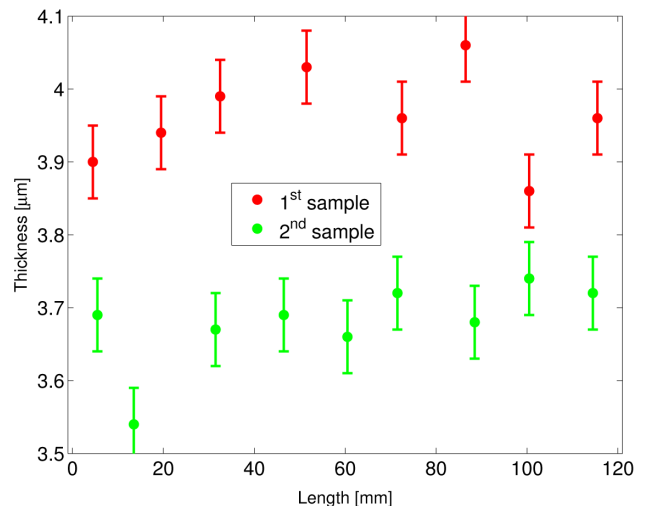

FIG. 4. Measurements of the NEG coating thickness on the two copper slabs used for the experiments.
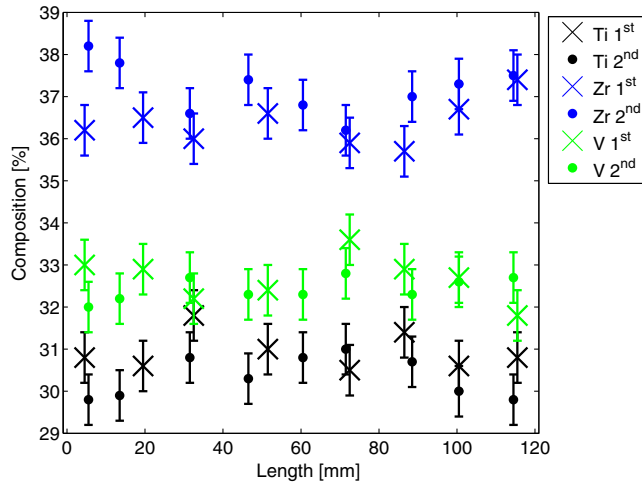
FIG. 5. Measurements of the NEG coating composition on the two copper slabs used for the experiments.

FIG. 7. Electric field of the first two degenerate modes inside a square waveguide and sum (right) of the first two modes propagating when a slab is placed in the center.

The assumption of single mode propagation is justified in Sec. IV.

III. THE ANALYTICAL METHOD

A. Relative attenuation: General formulation

In this section, we give the general definition of attenuation in a waveguide and evaluate it in the specific case of the waveguide used for measurements.

The definition of the attenuation constant is expressed by the formula [28,29]:

$$\alpha(z) = -\frac{1}{2P}\frac{dP}{dz} \tag{4}$$

where P is the total power flow at z and $-dP$ is the power dissipated in a section of waveguide of length dz.

From Eq. (4), it follows that the attenuation constant due to losses on guide walls is

$$\alpha(z) = -\frac{1}{2}\frac{\mathrm{Re}[Z_S(z)]\int|H_{\mathrm{tan}}|^2 ds}{\mathrm{Re}[Z(z)]\iint|H_{\mathrm{t}}|^2 dS}, \tag{5}$$

where Z_S is the equivalent surface impedance and Z is the characteristic impedance of the propagating mode. H_{tan} and H_{t} are the nondissipative values of the magnetic field tangential to the guide periphery and transverse to the guide cross section, respectively. The line integral with respect to ds extends over the guide periphery, and the surface integral with respect to dS extends over the guide cross section.

We consider the propagation of the sole $TE_{1,1}$ mode in the cylindrical waveguide. The attenuation of this single mode in a generic waveguide is

$$A_{\mathrm{cyl}} = \frac{1}{2}\frac{\mathrm{Re}(Z_S)}{\mathrm{Re}(Z_{1,1})}\frac{\int_l|n\times H_{1,1}|^2 dl}{|I_{1,1}|^2}, \tag{6}$$

where $Z_{i,j}$ is the i, j mode impedance and $I_{i,j}$ is the relevant excitation current. To evaluate the attenuation in the pyramidal transition we consider the sum of two modes $TE_{1,0}$ and $TE_{0,1}$, the formula in this case is

propagation only is defined by the cutoff frequencies of $f_{TE_{1,1}} = 97.6$ GHz and $f_{TE_{1,2}} = 282.6$ GHz.

In order to complete the model, one has to take into account the presence of the two integrated antennas for signal collection and detection. Since the half-aperture of each pyramidal horn is $< 5°$ we may consider that the modes propagate in a locally uniform square waveguide and take the relevant lower modes. The first two modes, having the same cutoff frequency, are degenerate. If their excitation coefficient has the same amplitude, their sum will exhibit an electric field everywhere orthogonal to the horizontal diagonal, where we are going to put the slab, as shown in Fig. 7.

Doing the same considerations as for the cylindrical waveguide and considering a minimum side of $0.9\sqrt{2}$ mm (see Table I), the sum of the first two modes allowed to pass have a cut off frequency of $f_{TE_{1,0}} = f_{TE_{0,1}} = 117.8$ GHz. The other two modes allowed to pass start their propagation from $f_{TE_{2,1}} = f_{TE_{1,2}} = 263.3$ GHz.

Therefore, taking into account the propagation in both the transitions and in the circular waveguide, the overall usable frequency window for a single mode propagating inside the DUT ranges from 118 GHz to 283 GHz.
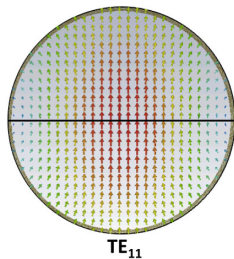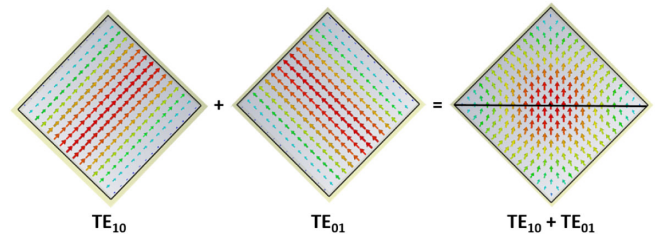

FIG. 6. First mode propagating inside the cylindrical waveguide with a slab placed in the center.

$$A_{\mathrm{pyr}} = \frac{1}{2}\mathrm{Re}(Z_S)\frac{\int_l |n \times (H_{1,0} + H_{0,1})|^2 dl}{\mathrm{Re}(Z_{1,0})|I_{1,0}|^2 + \mathrm{Re}(Z_{0,1})|I_{0,1}|^2}. \quad (7)$$

The explicit analytical expression of the modes is reported in Appendix A.

In the case of coating material, the expression of Z_S, which has to be inserted in Eqs. (6) and (7), is

$$Z_S = Z_{\mathrm{coat}}\frac{Z_{\mathrm{cu}} + jZ_{\mathrm{coat}}\tan(k_{\mathrm{coat}}d)}{Z_{\mathrm{coat}} + jZ_{\mathrm{cu}}\tan(k_{\mathrm{coat}}d)}, \quad (8)$$

where d is the coating thickness. When $d = 0$ there is no coating and $Z_S = Z_{\mathrm{cu}}$.

The characteristic impedance in the Leontovich approximation for a metallic case ($\epsilon'' \gg \epsilon'$) is [28]

$$Z = (1+j)\sqrt{\frac{\omega\mu}{2\sigma}} = \frac{1+j}{\sigma\delta} \quad (9)$$

and the propagation constant in the same condition is

$$k = (1-j)\sqrt{\frac{\sigma\omega\mu}{2}} = \frac{1-j}{\delta}, \quad (10)$$

where δ is the skin-depth defined as

$$\delta = \sqrt{\frac{2}{\sigma\omega\mu}} \quad (11)$$

and where μ is the total permeability, $\omega = 2\pi f$ and σ the material conductivity.

As stated in Eq. (3), the procedure consists in the measurement and in the analytical/numerical evaluation of the relative attenuation defined as

$$RA \triangleq A^{\mathrm{coat}} - A^{\mathrm{cu}}. \quad (12)$$

With the above definition we do not need to evaluate the attenuation on the walls but only on the slabs.

B. Estimation on the slab in the cylindrical waveguide

The first mode in the cylindrical waveguide with a slab placed in the center is shown in Fig. 6. The attenuation constant on the slab placed in the center of a cylindrical waveguide is:

$$\alpha_{\mathrm{cyl}} = 4\mathrm{Re}(Z_S)\frac{\chi'_{1,1}k_{z_{1,1}}}{\pi a_0 Z_0 k_0 (\chi'^2_{1,1} - 1)J_1^2(\chi'_{1,1})}$$

$$\times \left[\frac{k_{t_{1,1}}^2}{k_{z_{1,1}}^2}\int_o^{\chi'_{1,1}}|J_1(u)|^2 du + \int_o^{\chi'_{1,1}}|J'_1(u)|^2 du\right], \quad (13)$$

where Z_0 is the characteristic impedance in the free space, a_0 is the radius of the waveguide. J_1 and J'_1 are the first order Bessel function and its derivative respectively. The quantity $\chi'_{1,1}$ is the first nonvanishing root of the equation:

$$J'_1(x) = 0$$

and

$$k_0 = \frac{\omega}{c}; \qquad k_{t_{1,1}} = \frac{\chi'_{1,1}}{a_0}; \qquad k_{z_{1,1}} = \sqrt{k_0^2 - k_{t_{1,1}}^2}.$$

The explicit analytical expression of the quantity in square brackets of Eq. (13) is given in closed form in Appendix B. The total attenuation along the slab of length l_g is described by the formula:

$$A_{\mathrm{cyl}} = \int_0^{l_g}\alpha_{\mathrm{cyl}}dz = \alpha_{\mathrm{cyl}}l_g \quad (14)$$

where l_g is the length of the waveguide.

The relative attenuation [see Eq. (12)] for the cylindrical waveguide is

$$RA_{\mathrm{cyl}} \triangleq A_{\mathrm{cyl}}^{\mathrm{coat}} - A_{\mathrm{cyl}}^{\mathrm{cu}}. \quad (15)$$

Using CST simulations (frequency solver and coating tool) [24] we can evaluate the difference between the analytical formula [Eq. (15)] and the electromagnetic full wave simulations for various thicknesses of the NEG coating in the cylindrical waveguide. Frequency domain simulations have been performed by imposing the first mode propagation and comparing the scattering parameter, S_{21}, to evaluate the attenuation. We used an estimated NEG conductivity value of $\sigma_{\mathrm{coat}} = 3.5 \times 10^5$ S/m, as reported in [22]. The agreement between the results of Eq. (15) and the CST tool is excellent and underlines the reliability of the analytical tool (see Fig. 8).
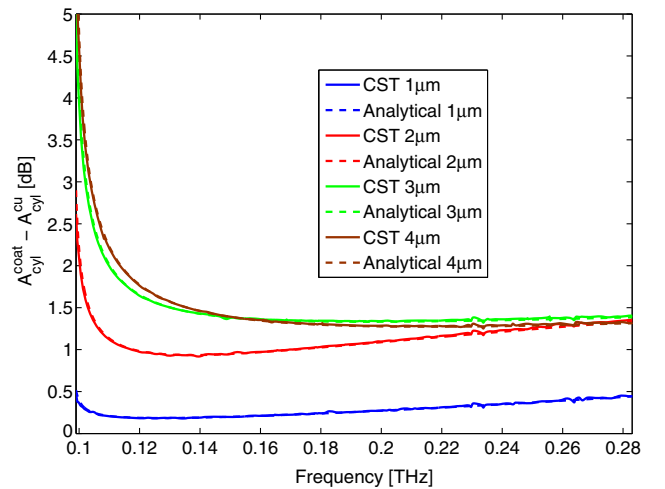

FIG. 8. Cylindrical waveguide: relative attenuation of the first mode on the slab for different coating thicknesses with $\sigma_{\mathrm{coat}} = 3.5 \times 10^5$ S/m. Comparison between analytical formulas (dashed line) and CST frequency domain simulations (full line).

C. Estimation on the slab in the pyramidal transitions

The slab placed in the center of the pyramidal transitions forces the first two degenerate modes to sum-up because of the boundary conditions on the metallic slab (see Fig. 7).

Differently from the contribution in the cylindrical section, the attenuation on the slab given by the symmetric input and output transitions is not constant, since the antenna aperture changes along the horn length. The total attenuation per unit length is

$$\alpha_{\mathrm{pyr}}(z) = \sqrt{2} \frac{\mathrm{Re}(Z_S) k_{z_{\mathrm{sum}}}(z)}{a(z) Z_0 k_0} \left[1 + \frac{2 k_{t_{\mathrm{sum}}}^2(z)}{k_{z_{\mathrm{sum}}}^2(z)} \right], \quad (16)$$

where

$$k_{t_{\mathrm{sum}}}(z) = \frac{\pi}{a(z)}; \qquad k_{z_{\mathrm{sum}}}(z) = \sqrt{k_0^2 - k_{t_{\mathrm{sum}}}^2(z)}$$

and

$$a(z) = b + zd = b + \frac{z(B-b)}{l_t}$$

expresses how the side of the horn changes along the transition. l_t is the longitudinal length of the transition, b and B are the side dimension of the exit and entrance of the pyramidal horn transition. The attenuation of two modes on the slab in the pyramidal transitions is given by the integral:

$$A_{\mathrm{pyr}} = 2 \int_0^{l_t} \alpha_{\mathrm{pyr}}(z) dz. \quad (17)$$

Where the factor 2 indicates that the attenuation is the same for the two pyramidal transitions. The explicit

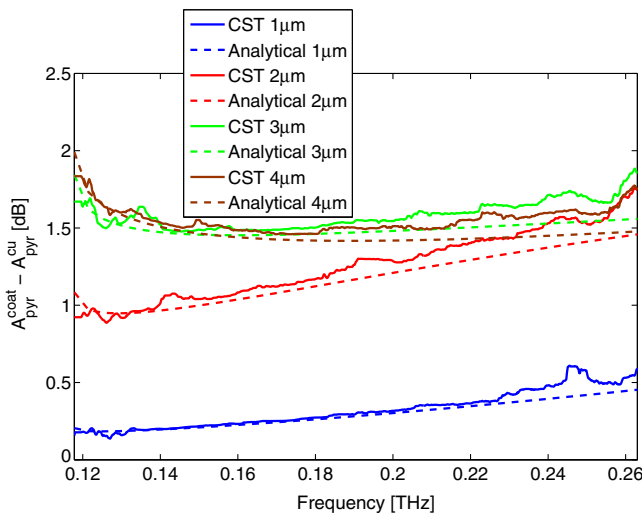FIG. 9. Pyramidal transitions: relative attenuation of the sum of the first two modes on the slab for different coating thicknesses with $\sigma_{\mathrm{coat}} = 3.5 \times 10^5$ S/m. Comparison between analytical formulas (dashed line) and CST frequency domain simulations (full line).
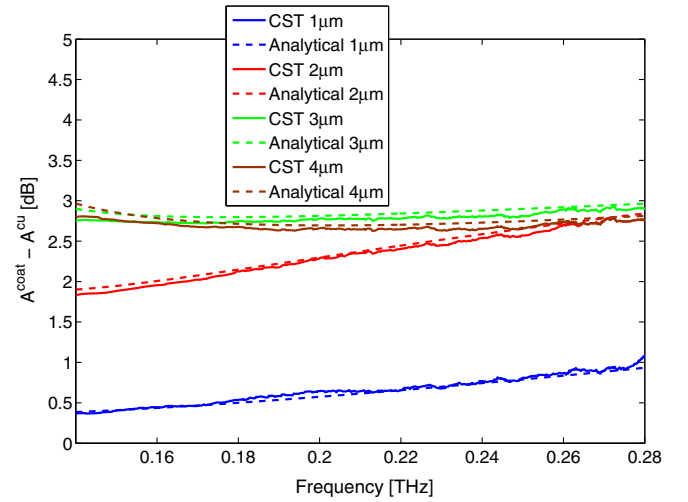

FIG. 10. DUT: relative attenuation of propagating mode on the slab for different coating thicknesses with $\sigma_{\mathrm{coat}} = 3.5 \times 10^5$ S/m. Comparison between analytical formulas (dashed line) and CST frequency domain simulations (full line).

evaluation of Eq. (17) in closed form is given in Appendix B. As for the cylindrical waveguide, we evaluate the relative attenuation [see Eq. (12)] for the pyramidal transition as

$$RA_{\mathrm{pyr}} \stackrel{\triangle}{=} A_{\mathrm{pyr}}^{\mathrm{coat}} - A_{\mathrm{pyr}}^{\mathrm{cu}}. \quad (18)$$

The relative attenuations evaluated analytically [Eq. (18)] and with CST frequency domain solver are compared in Fig. 9 for different thicknesses with $\sigma_{\mathrm{coat}} = 3.5 \times 10^5$ S/m. The simulations are performed with two pyramidal transitions put back to back on the smaller side. Also for this case the agreement simulation-analytical data is really good.

D. Estimation on the slab in the DUT

The total relative attenuation along the entire DUT is analytically evaluated as the sum of Eqs. (15) and (18), whose values are reported in Figs. 8 and 9. As described in Sec. II B, we neglect the contribution to losses given by further modes in the transition between the pyramidal horns and the cylindrical waveguide. Therefore, the comparison with CST simulations on the overall assembled structure for various coating thicknesses ($\sigma_{\mathrm{coat}} = 3.5 \times 10^5$ S/m) is an effective way to test the validity of this assumption. The very good agreement shown in Fig. 10, confirms the possibility of neglecting any mode conversion inside the horn or along the transition in the analytical model.

IV. SUB-THz SYSTEM

Sub-THz measurements are carried out using a time domain spectrometer (TDS) operating in transmission mode. The setup is based on a commercial THz-TDS system (TERA K15 by MENLO systems) customized for

the waveguide characterization. The system is driven by a femtosecond fiber laser @1560 nm with an optical power of < 100 mW and a pulse duration < 90 fs. In the standard configuration, the laser output splits into two beams in pump-probe mode. Fiber-coupled photoconductive antenna modules are utilized for both electric field signal emission and detection. A fast opto-mechanical line with a maximum scanning range of approximately 300 ps is used to control the time delay between the pump and the probe beam. Signal detection is performed by a lock-in amplifier that drives the pulse generation at about 90 KHz and integrate the output voltage over an interval of 100 ms. Pulse waveforms are sampled by 2048 data-points in 150 fs intervals of optical delay (step size ~30 μm). Each scan requires about 10 min of measurement time.

The THz beam system has a set of symmetric optics with respect to the center line between the transmitter and the receiver. In particular, TPX (polymethylpentene) lenses are used to collimate the short (1–2 ps) linearly polarized pulse on the waveguide. This results in a Gaussian-like beam with a waist of approximately 8 mm in diameter and a quasi-plane wave phase front. The coupling efficiency between the free space signal and the input and output horns is then mechanically optimized by maximizing the signal transmitted through the DUT. In order to understand if there is any effect on the signal produced by the excitation of higher order modes, we evaluate in Appendix C the ratio between the field amplitude coefficients of the first and second order modes as a function of the beam spot size. Under our experimental conditions, we can safely assume that we work in a single mode regime and that the mode conversion at the entrance of the horn antennas may be neglected.

A sketch of the optical configuration is shown in Fig. 11.
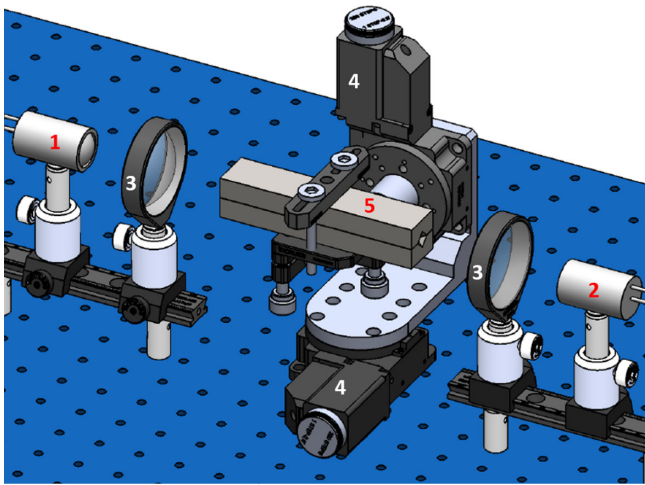

FIG. 11. Sketch of the opto-mechanical setup utilized for the measurements: (1) emitter, (2) detector, (3) TPX collimating lenses, (4) micrometric alignment systems, (5) DUT (waveguide).
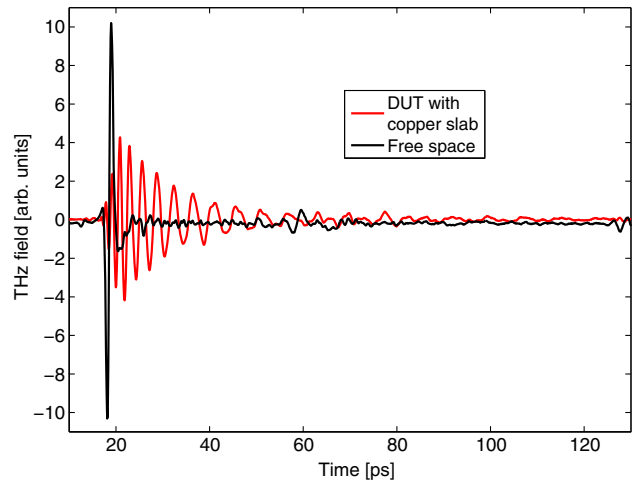

FIG. 12. THz time domain signal propagation in free space (black curve) and in the DUT (red curve).

For an accurate control over the target positioning, the waveguide is placed on a kinematic mount coupled with a micrometric goniometer. The base part of the waveguide is fixed onto the kinematic mount and the metal slabs are replaced by removing the top part of the waveguide structure only. To minimize any possible optical gap in between the top and the base plate, the waveguide is firmly tightened with a rigid clamp. To block any unwanted THz radiation from the emitter antenna, the area around the waveguide entrance is shielded with a metal sheet with an extrude cut at the center. Figure 12 shows the THz time domain signals obtained in free space and in the DUT, with the input beam polarized parallel to the waveguide slab. In the latter case, the ps-scale input pulse is broadened to more than 50 ps and strongly reshaped by the reflections inside the waveguide. The stretching of the transmitted signal, compared with the free space input pulse, is due to the strongly dispersive character of the waveguide, that acts as a delay line [30].

Frequency dependent transmission curves are obtained through the application of a standard fast Fourier transform (FFT) algorithm. In the experiment, the maximum frequency resolution is about 4 GHz, limited by the scanning range of the delay line only.

V. MEASUREMENT RESULTS

We tested two copper slabs coated with NEG having 3.96 μm and 3.68 μm average thickness and a bare copper slab. For all three samples we performed five different measurements replacing the slab each time, in order to reduce the unavoidable uncertainty given by the measurement procedure. After data averaging, the related error is reduced, nevertheless it is much larger than the statistical fluctuations coming from the TDS performance (laser stability, mechanical vibrations, environment noise, etc.).
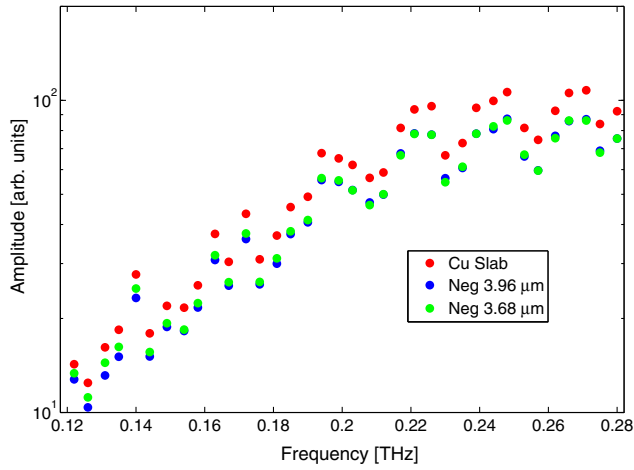
FIG. 13. Frequency spectrum showing the averaged amplitude data for the three samples: copper slab (red dots), NEG coated slab 3.96 μm (blue dots) and NEG coated slab 3.68 μm (green dots).

The mean amplitude spectrum derived by the FFT analysis is shown for each sample in Fig. 13 in the frequency range of our interest. The data show that the attenuation on the two NEG coated samples (blue and green dots) is constantly larger than on the copper slab (red dots). Moreover, losses tend to increase with higher frequency, likely indicating a reduction of the skin depth to values smaller than the coating thickness. Furthermore, at the lowest frequencies, the noise distorts the signal and can introduce artificial phase discontinuities, making the phase unwrapping difficult and producing artifacts in the data spectrum [31]. For this reason, we discarded the data below 160 GHz, and in the following, all results are presented in the range 160–283 GHz.

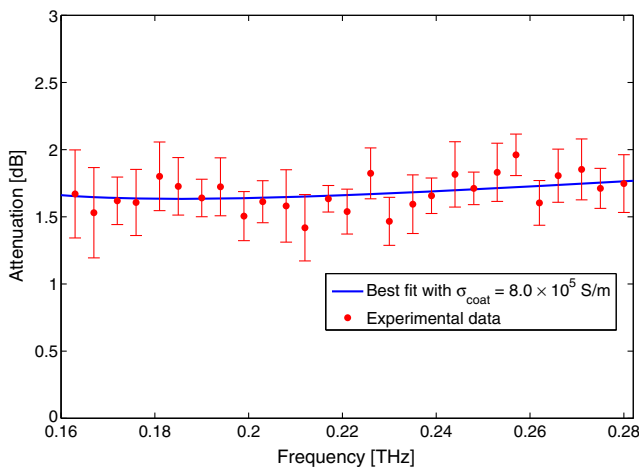The experimental results are then compared with mathematical model based on the theory described in Sec. III as function of the coating conductivity resorting to Eqs. (15) and (18).

In Fig. 14, the measurements for the 3.96 μm coating are shown. From the best fit, we get the value $\sigma_{coat} = (8.0 \pm 0.4) \times 10^5$ S/m and a value of 0.40 for the reduced χ^2.

Similarly, in Fig. 15 the same results are shown for the 3.68 μm coating. In this case, the estimated value of σ_{coat} is $(8.2 \pm 0.6) \times 10^5$ S/m and reduced χ^2 is equal to 0.36.

As expected, given the similar thickness, the two NEG coatings show the same value for the estimated conductivity, within the error determined by the fitting procedure. It is worthwhile to note that such value is also in good agreement with previous results obtained for the same alloy and measured using the frequency domain approach [22]. Using CST, one can also evaluate the effect of the sample roughness on the estimate of NEG conductivity.

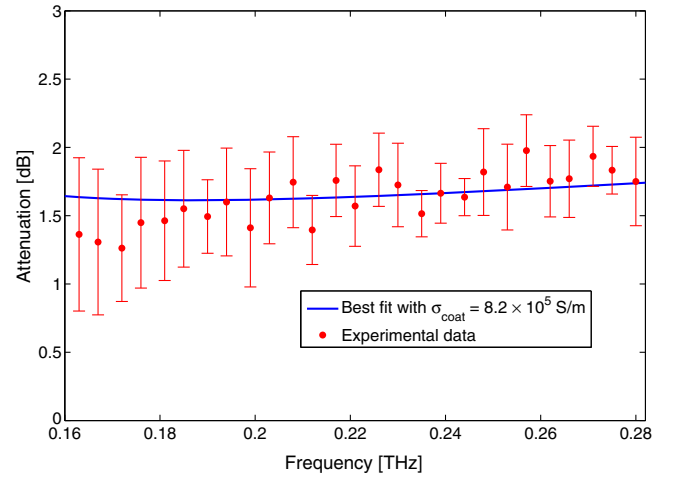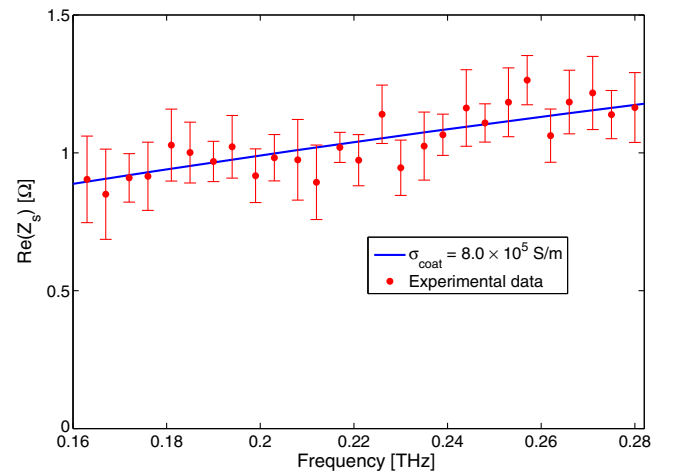
FIG. 15. Attenuation on the NEG coated slab of 3.68 μm: averaged experimental data (red dots) and best fit curve (blue). The value of reduced $\chi^2 = 0.36$.

FIG. 14. Attenuation on the NEG coated slab of 3.96 μm: averaged experimental data (red dots) and best fit curve (blue). The value of reduced $\chi^2 = 0.40$.
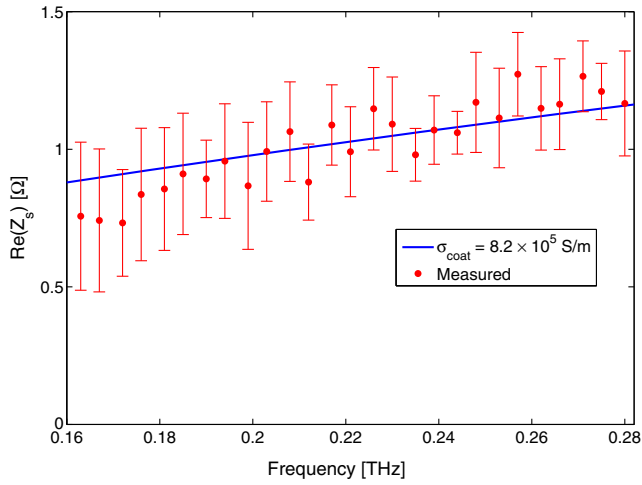

FIG. 16. Surface impedance estimation of the 3.96 μm NEG coated slab: from averaged experimental data (red dots) and from best fit curve conductivity (blue).

FIG. 17. Surface impedance estimation of the 3.68 μm NEG coated slab: from averaged experimental data (red dots) and from best fit curve conductivity (blue).

Following [22,32], we assume for our samples a roughness average value of 0.2 μm, which gives a maximum reduction in conductivity of the order of 7%. This value lies within the measurement error band in our frequency range. Nevertheless, it is worthwhile to observe that the roughness cannot be neglected at higher frequencies.

The final step, presented in Figs. 16 and 17, is the evaluation of the real part of the surface impedance, see Eq. (8), in the same frequency range.

VI. CONCLUSIONS

We developed a novel EMC system for time domain measurements that allows us to evaluate the surface impedance of materials used for coating in accelerator beam pipes in a fairly broad frequency window in the sub-THz range. Unlike frequency domain measurements, this method allows to evaluate the electromagnetic properties of samples under test in a simple and handy way. The advantages of this setup, based on a tailored waveguide with a central coated slab, are mainly the possibility to characterize uniform samples and the reusability of the DUT for different coating materials, as the a-C.

The comparison between the theoretical evaluation and the numerical solution shows very good agreement. The developed analytical method is robust.

From time domain measurements, we are able to estimate the conductivity of the NEG coating, yielding for the two samples the same value within the error given by the best-fitting procedure. Our results well agree with previous data obtained with the frequency domain approach. Using the determined σ_{coat} we can evaluate in a very simple way the real part of the surface impedance as a function of frequency for relatively large area samples, which in turn can be eventually used for the modeling of beam impedance in modern accelerators.
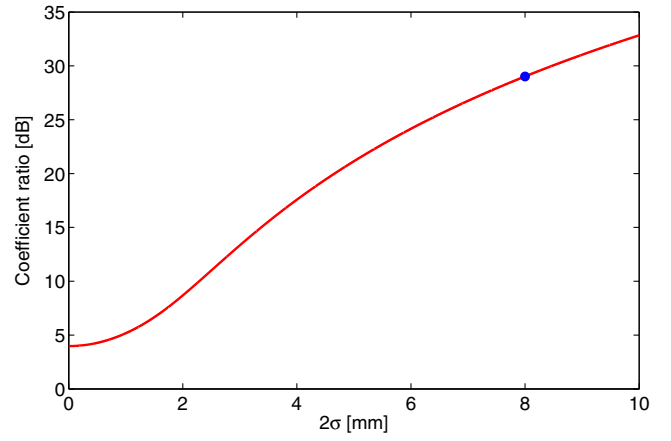

FIG. 18. Ratio between the first and the second mode expansion coefficients as a function of the beam spot size (2σ).

APPENDIX A

The field components used in Eq. (6) for the cylindrical waveguide, where only the mode TE$_{1,1}$ propagates, are:

$$H_{r_{1,1}} = H_{r_{1,1}}(r,0) = I_{1,1}\sqrt{\frac{2}{\pi}}\frac{\chi'_{1,1}}{a\sqrt{\chi'^2_{1,1}-1}}\frac{J'_1(\frac{\chi'_{1,1}r}{a})}{J_1(\chi'_{1,1})} \qquad (A1)$$

$$H_{z_{1,1}} = H_{z_{1,1}}(r,0) = -j\frac{k_{t_{1,1}}}{k_{z_{1,1}}}I_{1,1}\sqrt{\frac{2}{\pi}}\frac{\chi'_{1,1}}{a\sqrt{\chi'^2_{1,1}-1}}\frac{J_1(\frac{\chi'_{1,1}r}{a})}{J_1(\chi'_{1,1})}. \qquad (A2)$$

The field components used in Eq. (7) for the pyramidal transitions are

$$H_{x_{1,0}} = I_{1,0}\frac{\sqrt{2}}{a}\cos\left(\frac{\pi}{a}x\right) \qquad (A3)$$

$$H_{y_{1,0}} = I_{1,0}\frac{\sqrt{2}}{a}\cos\left(\frac{\pi}{a}y\right) \qquad (A4)$$

APPENDIX B

The analytical expression of the quantity in square brackets of the attenuation on the slab placed in the center of a cylindrical waveguide, Eq. (13), shown in Sec. III B is

$$\left[\frac{k_{t_{1,1}}^2}{k_{z_{1,1}}^2}\int_o^{\chi'_{1,1}}|J_1(u)|^2 du + \int_o^{\chi'_{1,1}}|J'_1(u)|^2 du\right] = \left[\frac{k_{t_{1,1}}^2}{k_{z_{1,1}}^2}\frac{\chi'^3_{1,1}}{12}\,_2F_3\left(\frac{3}{2},\frac{3}{2};2,\frac{5}{2},3;-\chi'^2_{1,1}\right) + J_0(\chi'_{1,1})\left(J_1(\chi'_{1,1}) - \frac{1}{2}J_0(\chi'_{1,1})\chi'_{1,1}\right)\right.$$

$$+ \frac{\chi'_{1,1}}{4}\,_2F_3\left(\frac{1}{2},\frac{1}{2};1,1,\frac{3}{2};-\chi'^2_{1,1}\right) + \frac{\chi'^3_{1,1}}{12}\,_2F_3\left(\frac{3}{2},\frac{3}{2};1,\frac{5}{2},3;-\chi'^2_{1,1}\right)$$

$$\left.+ \frac{\chi'^5_{1,1}}{1280}\,_2F_3\left(\frac{5}{2},\frac{5}{2};5,\frac{7}{2},5;-\chi'^2_{1,1}\right)\right] \tag{B1}$$

where $_2F_3(\alpha,\beta;\gamma,\delta,\epsilon;z)$ is a generalized hypergeometric function.

The analytical expression of the attenuation on the slab placed in the center of two pyramidal horns shown in Sec. III C is given by:

$$A_{\text{pyr}} = 2\int_0^{l_t}\alpha_{\text{pyr}}(z)dz = \sqrt{2}\frac{\text{Re}(Z_s)}{Z_0}\left\{-\frac{1}{2d}\log\left[\frac{\sqrt{1-(\frac{\pi}{k_0B})^2}-1}{\sqrt{1-(\frac{\pi}{k_0B})^2}+1}\frac{\sqrt{1-(\frac{\pi}{k_0a})^2}+1}{\sqrt{1-(\frac{\pi}{k_0a})^2}-1}\right] + \frac{2}{d}\left[\sqrt{\left(\frac{\pi}{k_0B}\right)^2}-\sqrt{\left(\frac{\pi}{k_0a}\right)^2}\right]\right\} \tag{B2}$$

APPENDIX C

The field distribution at the horn entrance is expanded as a sum of the modes pertaining to the square waveguide with a PEC slab on one diagonal [28]. The expansion coefficients, normalized to the total power carried out by the beam, can be obtained exploiting the orthogonality property of the modes. In Fig. 18 the ratio (in dB) between the first (sum $TE_{1,0}$ and $TE_{0,1}$) and the second (sum $TE_{2,1}$ and $TE_{1,2}$) mode expansion coefficients is reported as a function of the beam spot size (2σ). Within the experimental error, one can see that for a Gaussian-like beam with a waist of approximately 8 mm in diameter, as described in Section IV, this ratio turns out to be around 30 dB, definitively excluding any effect on the attenuation produced by the excitation of higher order modes.

[1] M. A. Furman, in *Proceedings, 5th Workshop on Electron-Cloud Effects (ECLOUD'12): La Biodola, Isola d'Elba, Italy, 2012* (2013); Electron cloud effects in accelerators, arXiv:1310.1706.

[2] G. Rumolo, F. Ruggiero, and F. Zimmermann, Simulation of the electron-cloud build up and its consequences on heat load, beam stability, and diagnostics, Phys. Rev. ST Accel. Beams **4**, 012801 (2001).

[3] R. Cimino, L. A. Gonzalez, R. Larciprete, A. Di Gaspare, G. Iadarola, and G. Rumolo, Detailed investigation of the low energy secondary electron yield of technical Cu and its relevance for the LHC, Phys. Rev. ST Accel. Beams **18**, 051002 (2015).

[4] C. Yin Vallgren, G. Arduini, J. Bauche, S. Calatroni, P. Chiggiato, K. Cornelis, P. C. Pinto, B. Henrist, E. Métral, H. Neupert, G. Rumolo, E. Shaposhnikova, and M. Taborelli, Amorphous carbon coatings for the mitigation of electron cloud in the CERN Super Proton Synchrotron, Phys. Rev. ST Accel. Beams **14**, 071001 (2011).

[5] M. Taborelli, P. Chiggiato, P. Costa Pinto, and P. Cruikshank, Nine years of carbon coating development for the SPS upgrade: achievements and heritage, CERN Technical Report No. CERN-ACC-2016-0010, 2015.

[6] M. Palmer *et al.*, Electron cloud at low emittance in CesrTA, Conf. Proc. **C100523**, TUYMH02 (2010).

[7] C. Benvenuti, R. Calder, and O. Gröbner, Vacuum for particle accelerators and storage rings, Vacuum **37**, 699 (1987), special Issue Modern Vacuum Practice.

[8] C. Benvenuti, P. Chiggiato, F. Cicoira, and V. Ruzinov, Decreasing surface outgassing by thin film getter coatings, Vacuum **50**, 57 (1998), electronic Properties of Metal/Non-Metal Microsystems.

[9] P. Costa Pinto, J. Ahlbck, E. Al-Dmour, B. Brtov, M. Grabski, B. Holliger, S. Marques Dos Santos, V. Nistor, C. Pasquino, A. Sapountzis, M. Taborelli, and I. Wevers, Proceedings, 6th International Particle Accelerator Conference (IPAC 2015): Richmond, Virginia, USA, 2015 (2015), WEPHA019, https://inspirehep.net/record/1418048/export/hx.

[10] M. Migliorati, E. Belli, and M. Zobov, Impact of the resistive wall impedance on beam dynamics in the Future Circular e^+e^- Collider, Phys. Rev. Accel. Beams **21**, 041001 (2018).

[11] L.-F. Chen, C. Ong, C. Neo, V. Varadan, and V. K. Varadan, *Microwave Electronics: Measurement and Materials Characterization* (John Wiley & Sons, New York, 2004).

[12] A. R. Von Hippel, *Dielectric Materials and Applications* (Artech House on Demand, Norwood, 1954), Vol. 2.

[13] A. Hernandez, E. Martin, J. Margineda, and J. M. Zamarro, Resonant cavities for measuring the surface resistance of metals at X-band frequencies, J. Phys. E **19**, 222 (1986).

[14] M. W. Hyde, M. J. Havrilla, and P. E. Crittenden, A novel method for determining the R-card sheet impedance using the transmission coefficient measured in free-space or waveguide systems, IEEE Trans. Instrum. Meas. **58**, 2228 (2009).

[15] J. Booth, D. H. Wu, and S. M. Anlage, A broadband method for the measurement of the surface impedance of thin films at microwave frequencies, Rev. Sci. Instrum. **65**, 2082 (1994).

[16] R. Wu and M. Qian, A simplified power transmission method used for measuring the complex conductivity of superconducting thin films, Rev. Sci. Instrum. **68**, 155 (1997).

[17] L. Angrisani, G. Cavallo, A. Liccardo, G. P. Papari, and A. Andreone, in *New Trends and Developments in Metrology*, edited by L. Cocco (IntechOpen, Rijeka, 2016), Chap. 2.

[18] G. P. Kniffin and L. M. Zurk, Model-based material parameter estimation for terahertz reflection spectroscopy, IEEE Trans. Terahertz Sci. Technol. **2**, 231 (2012).

[19] M. Theuer and J. S. Melinger, High resolution waveguide terahertz time-domain spectroscopy, J. Infrared, Millimeter, Terahertz Waves **32**, 1267 (2011).

[20] M. Razanoelina, R. Kinjo, K. Takayama, I. Kawayama, H. Murakami, D. M. Mittleman, and M. Tonouchi, Parallel-plate waveguide terahertz time domain spectroscopy for ultrathin conductive films, J. Infrared, Millimeter, Terahertz Waves **36**, 1182 (2015).

[21] A. Khachatrian, J. S. Melinger, and S. B. Qadri, Waveguide terahertz time-domain spectroscopy of ammonium nitrate polycrystalline films, J. Appl. Phys. **111**, 093103 (2012).

[22] E. Koukovini-Platia, G. Rumolo, and C. Zannini, Electromagnetic characterization of nonevaporable getter properties between 220–330 and 500–750 GHz for the Compact Linear Collider damping rings, Phys. Rev. Accel. Beams **20**, 011002 (2017).

[23] E. Koukovini Platia, High frequency effects of impedances and coatings in the CLIC damping rings, Ph.D. thesis, Ecole Polytechnique, Lausanne, 2015.

[24] CST Microwave Studio—Getting started.

[25] J. F. Johansson and N. D. Whyborn, The diagonal horn as a sub-millimeter wave antenna, IEEE Trans. Microwave Theory Tech. **40**, 795 (1992).

[26] S. Silver, *Microwave Antenna Theory and Design*, Electromagnetic Waves (IET, Stevenage, 1983), p. 349.

[27] C. S. Lee, S. W. Lee, and S. L. Chuang, Plot of modal field distribution in rectangular and circular waveguides, IEEE Trans. Microwave Theory Tech. **33**, 271 (1985).

[28] N. Marcuvitz, *Waveguide Handbook*, IEEE Electromagnetic Waves (Peregrinus, London, 1986).

[29] G. Franceschetti, *Electromagnetics: Theory, Techniques, and Engineering Paradigms*, Springer Science & Business Media New York (Springer, New York, 1997).

[30] R. Mendis and D. M. Mittleman, Comparison of the lowest-order transverse-electric (TE1) and transverse-magnetic (TEM) modes of the parallel-plate waveguide for terahertz pulse applications, Opt. Express **17**, 14839 (2009).

[31] W. Withayachumnankul and M. Naftaly, Fundamentals of measurement in terahertz time-domain spectroscopy, J. Infrared, Millimeter, Terahertz Waves **35**, 610 (2014).

[32] A. Prodromides, Non-evaporable getter thin film coatings for vacuum applications, Ph.D. Thesis, LPHE, 2002.